

See discussions, stats, and author profiles for this publication at: <https://www.researchgate.net/publication/262456203>

# Solar Hydrogen Generation by a CdS–Au–TiO<sub>2</sub> Sandwich Nanorod Array Enhanced with Au Nanoparticle as Electron Relay and Plasmonic Photosensitizer

ARTICLE in JOURNAL OF THE AMERICAN CHEMICAL SOCIETY · MAY 2014

Impact Factor: 12.11 · DOI: 10.1021/ja503508g · Source: PubMed

CITATIONS

57

READS

103

8 AUTHORS, INCLUDING:



Jiangtian Li

West Virginia University

43 PUBLICATIONS 1,717 CITATIONS

SEE PROFILE



Peng Zheng

West Virginia University

9 PUBLICATIONS 256 CITATIONS

SEE PROFILE



Tess R. Senty

West Virginia University

11 PUBLICATIONS 385 CITATIONS

SEE PROFILE



Alan D Bristow

West Virginia University

108 PUBLICATIONS 1,493 CITATIONS

SEE PROFILE

# Solar Hydrogen Generation by a CdS-Au-TiO<sub>2</sub> Sandwich Nanorod Array Enhanced with Au Nanoparticle as Electron Relay and Plasmonic Photosensitizer

Jiangtian Li,<sup>†,||</sup> Scott K. Cushing,<sup>†,‡,||</sup> Peng Zheng,<sup>†</sup> Tess Senty,<sup>‡</sup> Fanke Meng,<sup>†</sup> Alan D. Bristow,<sup>‡</sup> Ayyakkannu Manivannan,<sup>§</sup> and Nianqiang Wu<sup>\*,†</sup>

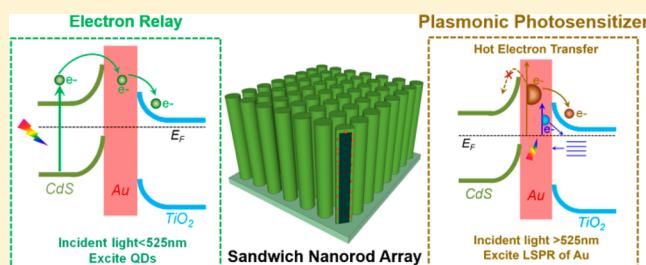
<sup>†</sup>Department of Mechanical and Aerospace Engineering, West Virginia University, Morgantown, West Virginia 26506-6106, United States

<sup>‡</sup>Department of Physics and Astronomy, West Virginia University, Morgantown, West Virginia 26506-6315, United States

<sup>§</sup>National Energy Technology Laboratory, U.S. Department of Energy, Morgantown, West Virginia 26507, United States

## Supporting Information

**ABSTRACT:** This paper presents a sandwich-structured CdS-Au-TiO<sub>2</sub> nanorod array as the photoanode in a photoelectrochemical cell (PEC) for hydrogen generation via splitting water. The gold nanoparticles sandwiched between the TiO<sub>2</sub> nanorod and the CdS quantum dot (QD) layer play a dual role in enhancing the solar-to-chemical energy conversion efficiency. First, the Au nanoparticles serve as an electron relay, which facilitates the charge transfer between CdS and TiO<sub>2</sub> when the CdS QDs are photoexcited by wavelengths shorter than 525 nm. Second, the Au nanoparticles act as a plasmonic photosensitizer, which enables the solar-to-hydrogen conversion at wavelengths longer than the band edge of CdS, extending the photoconversion wavelength from 525 to 725 nm. The dual role of Au leads to a photocurrent of 4.07 mA/cm<sup>2</sup> at 0 V (vs Ag/AgCl) under full solar spectrum irradiation and a maximum solar-to-chemical energy conversion efficiency of 2.8%. An inversion analysis is applied to the transient absorption spectroscopy data, tracking the transfer of electrons and holes in the heterostructure, relating the relaxation dynamics to the underlying coupled rate equation and revealing that trap-state Auger recombination is a dominant factor in interfacial charge transfer. It is found that addition of Au nanoparticles increases the charge-transfer lifetime, reduces the trap-state Auger rate, suppresses the long-time scale back transfer, and partially compensates the negative effects of the surface trap states. Finally, the plasmonic energy-transfer mechanism is identified as direct transfer of the plasmonic hot carriers, and the interfacial Schottky barrier height is shown to modulate the plasmonic hot electron transfer and back transfer. Transient absorption characterization of the charge transfer shows defect states cannot be ignored when designing QD-sensitized solar cells. This facile sandwich structure combines both the electrical and the optical functions of Au nanoparticles into a single structure, which has implications for the design of efficient solar-energy-harvesting devices.



## INTRODUCTION

Hydrogen generation by solar water splitting with a semiconductor photocatalyst presents a promising way to utilize renewable resources.<sup>1–4</sup> The solar-to-chemical energy conversion efficiency is heavily dependent upon light absorption, charge separation, charge migration, and charge recombination in photocatalysts, with an ideal semiconductor photocatalyst excelling in all four categories.<sup>5,6</sup> However, it has proven to be impossible to optimize a single semiconductor material for all these processes so far. Titanium oxide (TiO<sub>2</sub>) remains the most commonly used wide-band gap semiconductor photoanode in photoelectrochemical cells (PECs) due to its high catalytic activity, good stability, long minority diffusion length and low cost. However, it absorbs only ultraviolet light because the bandgap is 3.2 eV for anatase TiO<sub>2</sub>, limiting overall efficiency.<sup>7,8</sup> Doping with either transition metal or nonmetal ions can extend its light absorption into the visible light region, but

doping introduces trap states and charge carrier recombination centers, which limits the visible-light photocatalytic activity.<sup>8–12</sup>

Alternatively, wide-bandgap metal-oxide semiconductors can be combined with a narrow-bandgap semiconductor to form a heterostructure. This allows the excellent charge transport and recombination properties of the wide-bandgap semiconductor to be taken advantage of while simultaneously extending the light absorption range. For example, semiconductor quantum dots (QDs) have been commonly used as photosensitizers due to their high absorption cross-section and controllable absorption spectrum through nanoparticle radius.<sup>13–15</sup> Energetically favorable band alignment is necessary between the QD and the metal oxide in order to promote efficient interfacial charge transfer and chemical stability. Ideally, upon illumina-

Received: April 8, 2014

Published: May 16, 2014

tion, electrons excited in the QD transfer into the conduction band (CB) of the metal oxide while the holes transfer to the photoelectrode/electrolyte interface, extending the spectral range of the absorption without sacrificing recombination lifetimes.<sup>16</sup> In reality, slow electron injection and high charge recombination rates at the interfaces often remains problematic.<sup>17–21</sup> In organic dye-sensitized metal oxide electrodes, the photogenerated electrons quickly transfer into the metal oxide. However, the large density of surface trap states in QD-metal-oxide heterostructures and the subsequent charge accumulation at the surface slows down the transfer of excited electrons and holes, increasing the charge recombination rate and consuming the photogenerated charge carriers.<sup>23</sup> It is essential to promote efficient interfacial charge transfer from the QDs to the metal oxide to enable high efficiency energy conversion in QD-sensitized solar energy devices.

Another option for extending the light absorption of wide-bandgap semiconductors is to use plasmonic metal nanostructures as the photosensitizers instead of QDs. Localized surface plasmon resonance (LSPR) corresponds to the collective oscillation of surface electrons, with an oscillation frequency that is dependent on size, shape, and metal of the nanostructure. The energy stored in the plasmon can be transferred to a semiconductor<sup>24</sup> by direct electron transfer (DET)<sup>25</sup> or plasmon-induced resonant energy transfer (PIRET).<sup>26</sup> DET occurs through the transfer of plasmonic hot electrons over the interfacial Schottky barrier,<sup>25,27–31</sup> whereas PIRET occurs through nonradiative dipole–dipole coupling between the plasmon in the metal and electron–hole pairs in the semiconductor.<sup>26,32,33</sup> Unlike organic dyes and QDs which require energetically favorable band alignment for transfer, the energy transfer through PIRET is dependent on spectral overlap in the absorption spectrum.<sup>24,26,32</sup>

Photocurrent enhancement has already been observed in ternary heterostructures composed of QDs, Au nanoparticles, and metal-oxide semiconductor nanoparticles.<sup>34–38</sup> The plasmonic photosensitization effect has yet to be reported for this structure, and the mechanism of photoconversion enhancement by the Au nanoparticles in the ternary structures remains poorly understood. Additionally, while the charge-transfer rate in QD-metal-oxide heterostructures has been frequently measured, the resulting transfer mechanism is largely inferred from the average lifetime change in a multiexponential fit to the QD exciton bleach.<sup>39–46</sup> The uncertainty of multiple exponential fitting parameters has led to divergent reports of the electron-transfer time from femtoseconds to nanoseconds, although the relative change in lifetime with energy-barrier height is impressively consistent with predictions from Marcus theory.<sup>39–46</sup> Nevertheless, the inherently nonexponential nature of Auger decay and other recombination/transfer mechanisms in the semiconductor further blurs the charge-transfer mechanism when the measured rates are interpreted from the metal-oxide semiconductor's decay instead of the QD bleach. The acceptor dynamics are commonly found not to obey the first-order rate equation adapted from charge-transfer models suitable for dyes, as recently evidenced by the discoveries of Auger-based electron transfer and diffusion-based Auger recombination in the inverted Marcus region.<sup>47,48</sup> The difficulty in interpreting transient absorption measurements has led to ambiguity in how the charge transfer precedes once carriers have gone from the QD into the interfacial surface states, despite this being the critical step to charge separation. This ambiguity in interpretation can be overcome by inverting

the transient absorption data to provide rates and lifetime versus carrier density.

In the present work, a sandwich-structured CdS-Au-TiO<sub>2</sub> nanorod array, which is vertically aligned on a fluorine-doped tin oxide (FTO) substrate, acts as the photoanode in a PEC for solar hydrogen generation. Herein, the gold nanoparticles sandwiched between the TiO<sub>2</sub> nanorod and the CdS QD layer play a dual role in enhancing the solar-to-hydrogen conversion efficiency. First, the Au nanoparticles function as an electron relay that facilitates charge transfer between the CdS QDs and TiO<sub>2</sub>. Second, the Au nanoparticles act as a plasmonic photosensitizer that extends the photoconversion of the photoanode to 725 nm. The role of the Au nanoparticles is discerned using a newly adapted analysis method, which disentangles the multiple contributions to the transient absorption signals by directly mapping out the coupled rate equation which governs charge transfer. This procedure reveals the key role of the interfacial trap states in QD-metal-oxide heterostructures, in which the charge transfer can proceed through trap-state Auger scattering in the interface states with back transfer or increased charge separation occurring on the long-time scale.

When the Au nanoparticles are included in the heterostructure, the trap-based Auger-scattering rate is reduced, the transfer rate increases into the TiO<sub>2</sub>, and the back transfer is reduced independent of the excitation wavelength. The inverted transient absorption analysis reveals not only the dynamics of Au as a transfer channel but also its ability to overcome some of the deficiencies related with interfacial trap states in the CdS-TiO<sub>2</sub> heterostructures. Additionally, the plasmonic electron-transfer mechanism is identified as DET into the TiO<sub>2</sub>, with the transfer of hot electrons depending on the spectral position of the plasmon and the back-transfer dynamics depending on the hot electron distribution energy relative to the Schottky barrier. Understanding the mechanism of interfacial charge transfer in the CdS-TiO<sub>2</sub> heterostructure and the correlation with the PEC performance will assist in the tailoring of efficient QD-sensitized semiconductor heterostructures.

## ■ EXPERIMENTAL SECTION

**Synthesis of TiO<sub>2</sub> Nanorod Array on FTO.** The TiO<sub>2</sub> nanorod array was fabricated on the FTO substrate with a hydrothermal method.<sup>49,50</sup> Briefly, 0.8 g of titanium butoxide was dissolved into 60 mL of 6 M HCl aqueous solution and then transferred into a Teflon-lined steel autoclave with a capacity of 120 mL. The FTO substrates were placed against the Teflon wall with the FTO side facing down. The autoclave was heated in an oven at 150 °C for 24 h and then cooled down to room temperature. The TiO<sub>2</sub> nanorods were cleaned with deionized (DI) water and ethanol.

**Decoration of Au Nanoparticles on the TiO<sub>2</sub> Nanorods.** Ten mM HAuCl<sub>4</sub> aqueous solution was tailored to pH 4.5 with the NaOH solution. The TiO<sub>2</sub> nanorod array was immersed into the HAuCl<sub>4</sub> aqueous solution for 4 h.<sup>51</sup> The TiO<sub>2</sub> nanorod array was then washed with DI water and annealed at 450 °C for 2 h. This led to Au nanoparticles on the surface of TiO<sub>2</sub> nanorod.

**Fabrication of CdS-Au-TiO<sub>2</sub> Sandwich Structure.** CdS QDs were deposited on the surface of the Au-decorated TiO<sub>2</sub> nanorod array with a chemical bath deposition.<sup>50</sup> 1 M ammonia solution, 1 mM CdSO<sub>4</sub> and 5 mM thiourea were dissolved. The Au-TiO<sub>2</sub> nanorod array was then immersed into the CdS precursor solution and heated in a water bath at 60 °C for 10 min. After deposition of CdS, the nanorod array was washed with DI water and then annealed in a N<sub>2</sub> flow at 400 °C for 2 h.

**Characterization.** The morphology and structure of the nanorod array were observed with a field-emission scanning electron microscope (FE-SEM) (JEOL 7600F) and a transmission electron microscope (TEM, JEOL JEM 2100F). The UV–vis spectra were acquired with a Shimadzu 2550 UV–vis spectrometer under the diffuse-reflection model using an integrating sphere (UV 2401/2, Shimadzu). The chemical status of elements was analyzed with X-ray photoelectron spectroscopy (XPS, PHI 5000 Versa Probe system, Physical Electronics).

**Photoelectrochemical Performance Measurement.** In the PEC that was tested, an aqueous solution containing 0.25 M Na<sub>2</sub>S and 0.35 M Na<sub>2</sub>SO<sub>3</sub> (pH 12) was used as the electrolyte and bubbled with N<sub>2</sub> for 30 min prior to measurement. The nanorod array samples served as the photoanode. A Pt wire was employed as the counter electrode and Ag/AgCl as the reference electrode. A 300 W Xe lamp with an AM 1.5G filter was used as the light source. Band- and long-pass filters were used to adjust the wavelength region of incident light. The PEC performance was measured using a Gamry Reference 3000 Potentiostat/Galvanostat/ZRA Instrument.

The wavelength-dependent incident photo-electron conversion efficiency (IPCE) was measured with a 300W Xe lamp with an aligned monochromator (Oriol Cornstone 130 1/8m). The IPCE was calculated according to eq 1:<sup>52</sup>

$$\text{IPCE} = \frac{1240J}{\lambda I_{\text{light}}} \quad (1)$$

where  $J$  is the measured photocurrent density at 0 V versus Ag/AgCl at a certain wavelength ( $\lambda$ ), and  $I_{\text{light}}$  is the irradiance intensity at the specific wavelength ( $\lambda$ ).

Mott–Schottky (M-S) plots were obtained with a three-electrode cell at a ac frequency of 10 kHz using a ac amplitude of 10 mV. The capacitance was calculated from the electrochemical impedance spectra at a potential according to eq 2:<sup>52</sup>

$$Z_{\text{img}} = 1/2\pi fC \quad (2)$$

where  $Z_{\text{img}}$  is the imaginary part of the impedance,  $f$  is the frequency, and  $C$  is the capacitance. The M-S plots were then generated with the capacitance value normalized with surface area of the electrode.

The solar-to-chemical conversion efficiency ( $\eta$ ) was calculated according to eq 3:<sup>2</sup>

$$\eta = \frac{J_p(1.23 - |V|)}{I_0} \quad (3)$$

where  $V$  is the applied potential vs reversible hydrogen electrode (RHE),  $J_p$  is the photocurrent density at the measured potential, and  $I_0$  is the power density (100 mW/cm<sup>2</sup>). The potential versus RHE was calculated with a reference to Ag/AgCl according to the Nernst eq 4:

$$E_{\text{RHE}} = E_{\text{Ag/AgCl}} + 0.05916 \times \text{pH} + E_0 \quad (4)$$

where  $E_{\text{RHE}}$  is the potential vs RHE,  $E_{\text{Ag/AgCl}}$  is the measured potential vs Ag/AgCl, and  $E_0 = 0.1976$  V at 25 °C.

**Transient Absorption Measurements.** The 100 fs, 800 nm pulses of a 1 kHz Ti:sapphire amplifier were coupled into an optical parametric oscillator (OPA), then either frequency doubled in  $\beta$ -barium borate (BBO) to create a 400 nm pump or mixed with the OPA output to create a 480 nm pump by sum frequency generation. A pump power of 2 mW was used in both cases with a radius of  $\sim 200$   $\mu\text{m}$ . A white-light supercontinuum was created by tightly focusing the 800 nm output in a sapphire plate, using circular polarization to increase the stability. The white-light probe had a spot size of  $<100$   $\mu\text{m}$  and spanned 450–1000 nm, but wavelengths around 800 nm were excluded from the spectra because the continuum generated was strongly peaked at this wavelength beyond the dynamic range of the spectrometer, making acquisition unreliable in this region. White-light transient absorption spectroscopy was performed on the same samples used in the PEC testing. The data was converted by the inversion analysis (explained in the Supporting Information) to create plots of the time derivative of carrier density versus carrier density. The log–

log plot transforms  $(dN/dt) = -N^\alpha/\tau$  into  $\log(dN/dt) = -\alpha \cdot \log(N) - \log(1/\tau)$ , meaning that the relative position of the plotted data and the intercept determines the relaxation rate, while the slope gives the nonlinear order of the relaxation dynamics.

## RESULTS

**Microstructure.** Single-crystalline rutile TiO<sub>2</sub> nanorod arrays were grown on a FTO substrate with a hydrothermal process (Figure S3a).<sup>49,50</sup> The TiO<sub>2</sub> nanorods were  $\sim 2.5$   $\mu\text{m}$  high and 150–200 nm in a diameter (Figure 1b,c). Au

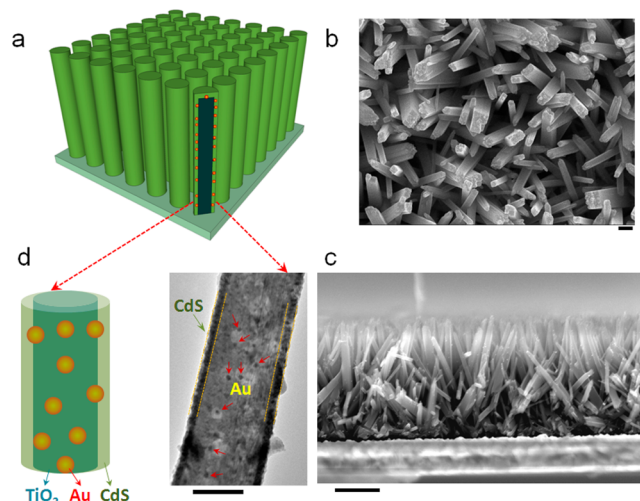


**Figure 1.** Microstructure of the CdS-Au-TiO<sub>2</sub> sandwich nanorod array. (a) Scheme for the sandwich nanorod array on the FTO substrate. (b) Top-view and (c) cross-section view of CdS-Au-TiO<sub>2</sub> nanorod array. (d) TEM image of a single sandwich nanorod. Scale bars: (b) 200 nm, (c) 1  $\mu\text{m}$ , and (d) 100 nm.

nanoparticles with an average size of  $11.5 \pm 3$  nm were deposited on the TiO<sub>2</sub> nanorod with a photoreduction method,<sup>51</sup> and a uniform 15 nm thick CdS QD layer was subsequently deposited with a chemical bath deposition method<sup>50</sup> to form a sandwich nanorod structure, as shown in Figures 1 and S3. This structure was also confirmed by the TEM and HRTEM images as well as the XPS analysis in Figures 1d and S4.

**Optical Absorption.** Figure 2 shows the UV–vis absorption spectra obtained from the TiO<sub>2</sub> nanorod array and the CdS-TiO<sub>2</sub> arrays in the absence and presence of Au

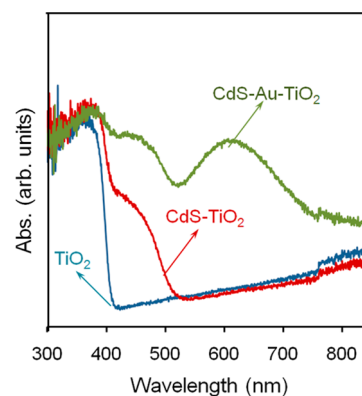


**Figure 2.** UV–vis absorption spectra obtained from the CdS-TiO<sub>2</sub> nanorod arrays with and without Au nanoparticles.



nanoparticles. The as-prepared TiO<sub>2</sub> nanorod array displayed a sharp absorption edge at around 410 nm, which matched the bandgap of rutile titanium dioxide. At longer wavelength, below the energy of the band gap of both TiO<sub>2</sub> and CdS-TiO<sub>2</sub>, the absorption had a background from the FTO. Sensitization of TiO<sub>2</sub> with the CdS QDs extended the absorption range up to 525 nm (2.36 eV). The presence of Au nanoparticles embedded between TiO<sub>2</sub> and CdS further increased the absorption at the wavelengths shorter than the band edge of CdS and extends the absorption range up to 725 nm. The strong absorption band centered at 610 nm corresponded to the LSPR of the Au nanoparticles. The LSPR peak was sensitive to the size, shape, and the surrounding environment.<sup>32</sup> For 10 nm spherical Au nanoparticles in an aqueous solution the LSPR peak is typically centered at 520 nm.<sup>32,51</sup> The LSPR peak red-shifted to 550 nm when the Au nanoparticles were deposited on the surface of TiO<sub>2</sub> (Figure S5). The LSPR peak of the Au nanoparticles sandwiched between the TiO<sub>2</sub> nanorod and the CdS QD layer further red-shifted to 610 nm due to the large refractive index of the CdS layer.

**Photoelectrochemical Performance.** Photoelectrochemical performance of the nanorod array photoanode was measured with a three-electrode cell with a Pt wire as the counter electrode and Ag|AgCl as the reference electrode. An aqueous solution containing 0.35 M Na<sub>2</sub>SO<sub>3</sub> and 0.25 M Na<sub>2</sub>S was used as the electrolyte. The CdS-TiO<sub>2</sub> nanorod array photoanode exhibited a photocurrent of 3.10 mA/cm<sup>2</sup> at 0 V (vs Ag|AgCl) under a full solar spectrum irradiation with simulated solar light at 100 mW/cm<sup>2</sup>. The CdS-Au-TiO<sub>2</sub> nanorod array photoanode showed a photocurrent as high as 4.07 mA/cm<sup>2</sup> under the same condition (Figure 3a). The solar-to-chemical energy conversion efficiency ( $\eta$ ) was calculated for the PEC with the CdS-Au-TiO<sub>2</sub> nanorod array photoanode. A maximum efficiency of ~2.8% was reached at -0.56 V (vs Ag|AgCl) under the simulated solar light radiation (Figure S6). The onset potential did not change for the binary CdS-TiO<sub>2</sub> and the ternary CdS-Au-TiO<sub>2</sub> systems. This indicated that the

Au nanoparticles, which were fully covered by the CdS QDs layer, did not change the surface chemistry of the photoanode.<sup>33,53</sup>

The IPCE spectrum was measured to correlate the energy conversion enhancement with the wavelength of the incident light (Figure 3b). Introduction of the Au nanoparticles into the nanorod array enhanced the IPCE substantially in the wavelength range from 325 to 725 nm. The IPCE at 375 nm was 85% and 52% for the nanorod arrays with and without Au nanoparticles, respectively. Figure 3c shows the IPCE enhancement factor as a function of the wavelength of incident light, which was obtained by dividing the IPCE value of CdS-Au-TiO<sub>2</sub> nanorod array with that of CdS-TiO<sub>2</sub> nanorod array at a given wavelength. There were two distinct enhancement wavelength regions in Figure 3c. In the wavelength range of 325–525 nm, the IPCE enhancement factor remained a constant of ~1.5. In the wavelength range of 525–725 nm, the IPCE enhancement factor increased significantly in the region of the plasmon. Its value was 5.8 at 625 nm and became 7 at 650 nm with a high tail at longer wavelengths. The high tail after 650 nm, represented by the dotted line, was an artifact of the division process due to the very low IPCE value (almost zero) of the CdS-TiO<sub>2</sub> photoanode at higher wavelengths (Figure 3c).

Introduction of Au nanoparticles into the semiconductor photoelectrodes has been previously reported to improve the performance of photoelectrodes by two possible mechanisms: (i) formation of a Z-scheme and (ii) negative shift of the Fermi level of Au-semiconductor heterostructure.<sup>54,55</sup> In the present study, the CdS-Au-TiO<sub>2</sub> nanorod array acted as the photoanode as illustrated in Figure S7, excluding the possibility of a Z-scheme. When Au nanoparticles are decorated on the semiconductor photoelectrode surface and are immersed into the liquid electrolyte, a negative shift of the Fermi level in the Au-semiconductor heterostructure occurs due to charge equilibration.<sup>54,55</sup> This results in a negative shift of both the onset potential in the *J*-*V* curve and the flat-band potential (apparent Fermi level).<sup>54,55</sup> In the present work, the onset potential in the *J*-*V* curve remained the same after the incorporation of Au nanoparticles into the photoanode, as observed in Figure 3a. In addition, the flat-band potential derived from Mott-Schottky plots in Figure 3d was -0.97 V (vs Ag|AgCl) for both CdS-TiO<sub>2</sub> and CdS-Au-TiO<sub>2</sub>. The lack of a negative shift excluded the Fermi-level equilibration as a possible enhancement mechanism. The lack of Fermi level equilibration was not surprising since the gold nanoparticles were fully covered with the CdS QDs layer, which isolated them from the liquid electrolyte.

#### Transient Absorption Analysis of Heterostructures.

White-light probe transient absorption spectroscopy was used to understand the various roles of Au nanoparticles in the heterostructure; see Figure S8. The differential absorption of TiO<sub>2</sub> was well characterized and exhibited the regions that corresponded to electron- and hole-trap state absorptions in the visible region,<sup>56–60</sup> while CdS showed a decrease in excited-state absorption at the exciton peak exhibiting a bleach.<sup>39–46</sup> Once an electron-hole pair was excited in the QD, the remaining charge density was reduced and less optical transitions can occur, diminishing the overall absorption (Figure S8). The presence of electron- and hole-trap absorption regions in TiO<sub>2</sub> at wavelengths longer than the bandgap can be understood as the excited carriers fill the defect states and open the possibility of new optical transitions (Figure S8).<sup>56–60</sup> The

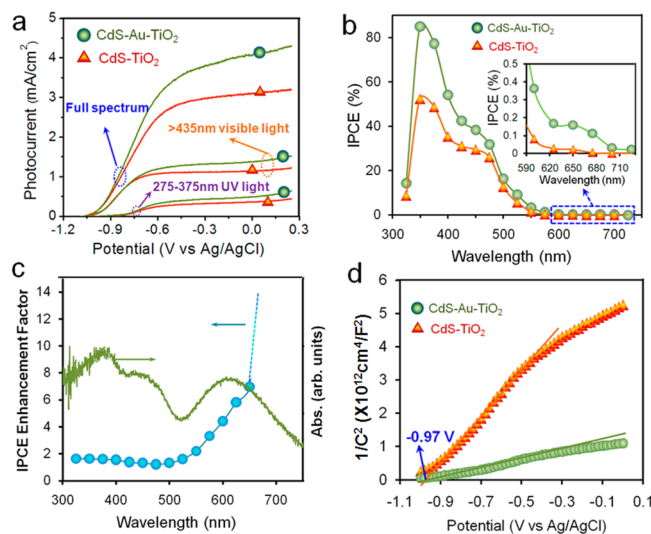


**Figure 3.** Photoelectrochemical performance of CdS-Au-TiO<sub>2</sub> nanorod array. (a) Photocurrent-applied potential (*J*-*V*) curves irradiated by full-spectrum of simulated solar light, visible light (>430 nm), and ultraviolet (275–375 nm), respectively. (b) Wavelength-dependent IPCE. (c) IPCE enhancement for the CdS-Au-TiO<sub>2</sub> nanorod array. (d) M-S plots for the CdS-TiO<sub>2</sub> and the CdS-Au-TiO<sub>2</sub> nanorod array.

spectral position of the defect states is similar to that seen in doped  $\text{TiO}_2$  (and other metal-oxide semiconductors where occupied midgap states exist), which leads to absorption at wavelengths longer than the band-edge.<sup>8</sup> The measured trap-state absorption is predominantly assigned to surface states, because the resulting signal is easily suppressed using electron and hole scavengers.<sup>56–60</sup>

The excited CdS bleach and  $\text{TiO}_2$  absorption are shown in Figure S9a,b. The spectral region of the transient absorption signal for electron- and hole-trap states and free carrier absorption (FCA) have also been shown as defined previously.<sup>60</sup> In the CdS- $\text{TiO}_2$  heterostructure, the signals from  $\text{TiO}_2$  and CdS did not overlap spectrally (Figure S9c), allowing for the electron- and hole-transfer pathways to be measured independently and the charge-transfer mechanism to be mapped out. This contrasts with the time-resolved fluorescence or single-wavelength transient absorption at the exciton bleach that only measure the CdS relaxation rate. Moreover, FCA only measures the dynamics of carriers once they have transferred into the bulk of the  $\text{TiO}_2$ . Hence, white-light transient absorption provides thorough insight into the charge transport out of the CdS QDs and charge transfer through the interfacial surface states concurrently, which is essential for understanding the long-lived charge transfer necessary for efficient PEC.

Simple exponential transfer models are insufficient for describing the complex dynamics of the heterostructures, where transport occur from donors, through traps, to acceptors and then back transfer, with each material having its own average lifetimes. As explained in Supporting Information, outside of the low injection limit, the decay dynamics of semiconductors depend nonlinearly on the excitation density. This dependence further precludes a simple exponential solution to the two-level rate equation describing the conduction and valence band of a single semiconductor, let alone the coupled rate equation governing the charge transfer in the heterostructure. Although analytical solutions exist to nonlinear rate equations, the mechanism must be known before hand to select the appropriate model, as several possible models will often accurately describe the decays. Therefore, multiple exponential fits are traditionally used to extract the charge-transfer time from the experimental pump–probe data since despite not being a direct solution to the decay kinetics, a fit to the data is almost always possible. While comparison of multiple exponential fitting parameters has been used to determine the change in average lifetime with heterostructuring, the loss of a direct connection to the underlying rate equation and the indeterminate nature of exponential fitting leads to a lack of mechanistic details and a large range of reported charge-transfer values.

To overcome these problems, we have adapted a data inversion analysis method as first proposed by Linnros<sup>61–63</sup> for single semiconductor systems using FCA, which does not rely on average lifetimes. The underlying principles and full procedure are discussed in Supporting Information. Briefly, instead of extracting the lifetime from a fit of the transient absorption decay, the derivative of the transient absorption data ( $dN/dt$ ) is taken numerically, inverting the measured data from the solution of the underlying rate equation back into the rate equation itself. If the donors and acceptors are both measured and analyzed in this manner, the governing rate equation for charge transfer in the coupled system is directly mapped out, revealing the underlying mechanism. Further, by dividing ( $dN/dt$ )

by the carrier density, the instantaneous lifetime is found independent of a fitting procedure. Both the instantaneous lifetime and carrier-relaxation rate have a characteristic dependence on carrier density that reveals the recombination mechanism, see Figures S10 and S11.

## DISCUSSIONS

**Mechanism of Charge Transfer in CdS- $\text{TiO}_2$ .** Figure 4 shows the transient absorption decays measured. The inverted

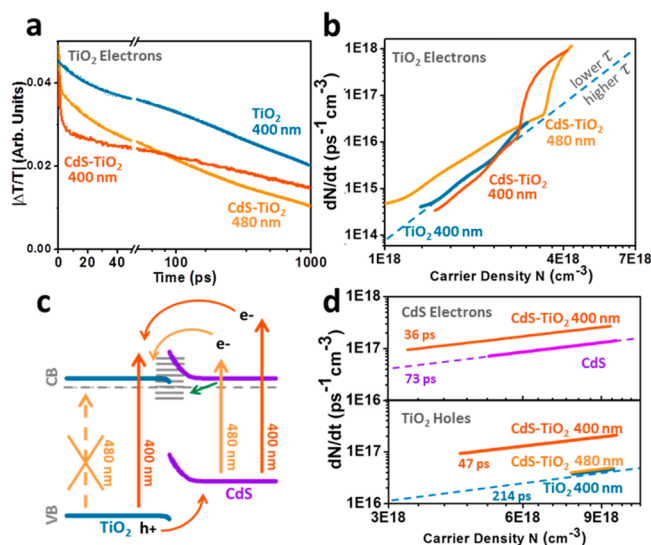


**Figure 4.** Relaxation dynamics in the CdS- $\text{TiO}_2$  heterostructure. (a) Transient absorption decay dynamics for  $\text{TiO}_2$  alone and CdS- $\text{TiO}_2$  with 400 and 480 nm excitation while probing the electron-trap states in  $\text{TiO}_2$ . (b) The inverted transient absorption decay shows the underlying form of the rate equation in the acceptor. (c) The charge transfer in the heterostructure can only be described if trap-state Auger scattering is included, green arrow. (d) The decrease in lifetime of the CdS probed at the band-edge bleach and  $\text{TiO}_2$  holes probed at the hole-trap states absorption is consistent with charge transfer out of the donor in the heterostructure. No change is seen for 480 nm excitation, consistent with no mobile holes being excited in the  $\text{TiO}_2$ .

transient absorption data are shown in Figure 4b,d for the CdS- $\text{TiO}_2$  heterostructure for 400 and 480 nm excitation with probe wavelengths from the white light supercontinuum selected to extract the response for the electron- and hole-trap states in  $\text{TiO}_2$  and the exciton in CdS. Data from CdS and  $\text{TiO}_2$  alone are shown for reference. The band alignment and expected electron/hole flow are shown in Figure 4c, estimated from a coupled Poisson and drift-diffusion calculation.<sup>64</sup> The difficulty in interpreting the exponential decays is mitigated once the data are inverted. On a log–log scale, a constant lifetime in the underlying rate equation shows up as a straight line with the linear dependence on the excited density and intercept corresponding to the inverse of the lifetime. A shift up or down of this line and the corresponding change in intercept indicates an increase or decrease in the rate, respectively. A change in slope of the derivative versus the carrier density corresponds to the nonlinear order of the nonlinear relaxation, as shown in Figure S10, which is unique for each possible relaxation mechanism.

The inverted data for the CdS-associated electrons and the  $\text{TiO}_2$ -associated trapped holes in the CdS- $\text{TiO}_2$  heterostructure show a decrease in lifetime (increase in rate) of the donors

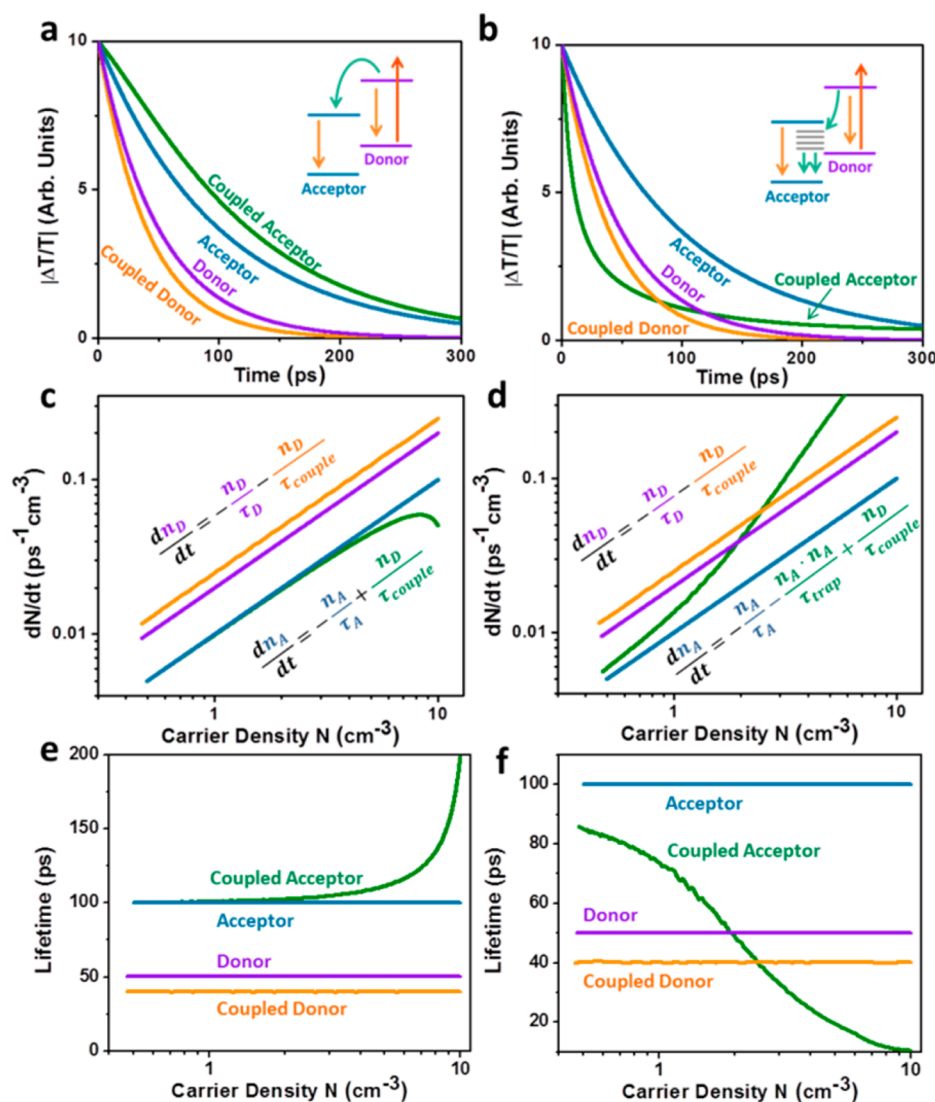


**Figure 5.** Modeled relaxation dynamics in heterostructures. The decay is shown for (a) a simple first-order coupled rate equation and (b) a coupled rate equation with trap-state Auger recombination in the acceptor. By taking the derivative of the respective decay dynamics, (c) and (d), the form of the underlying rate equation is seen. In both cases the donor has an initially higher rate due to charge transfer. The charge transfer into the acceptor leads to a lower initial rate (c) for the first-order coupled rate equation, but the addition of trap-state Auger scattering creates an initially higher relaxation rate (d). After charge transfer is complete the lifetime returns to that of the acceptor, as seen by the instantaneous lifetime in (e) and (f) found by inverting the rate equation of (c) and (d).

when pumped at 400 nm (Figure 4d). This reveals the carrier loss from the donors is described by a constant term like in a first-order rate equation on the time scales shown. Both decays are nonexponential on longer time scales, however the instantaneous lifetimes can be found by transforming the data to the original rate equation independent of fitting. Since the rate is a constant in the range of transfer, the instantaneous lifetime will be unaffected by changes in the time scale, allowing the transfer rate to be calculated. The transfer rates, found from the constant shift in lifetime before and after heterostructuring, are 70 and 60 ps for the CdS and TiO<sub>2</sub> hole-trap states for 400 nm excitation, respectively. These values are in agreement with the range of previously published data.<sup>39–46</sup> No change is seen in the hole lifetime for a 480 nm pump because although 480 nm light excites carriers directly into the hole traps in TiO<sub>2</sub> creating a transient absorption signal, these carriers are not mobile and are not energetically favorable for charge transfer due to their location mid gap. The CdS exciton bleach is also

not measured for 480 nm excitation due to the proximity of the pump to the band edge. The transfer times are summarized in the Supporting Information.

Next, the more complicated acceptor data were examined. The inverted data are shown for the TiO<sub>2</sub> electron-trap states in Figure 4b, with the dotted line extrapolating the TiO<sub>2</sub> decay. Rates above this line correspond to shorter lifetimes and below correspond to longer lifetimes, with the slope versus carrier density once again determining the nonlinear order of the relaxation mechanism. The instantaneous lifetime is shown in Figure S12. For 400 and 480 nm excitation, the initial relaxation rates reveal a faster electron transfer than in TiO<sub>2</sub> alone that is more similar to the faster charge-transfer times determined for the CdS exciton. At long time scale with 400 nm pump, the carrier lifetimes are greater than in TiO<sub>2</sub> alone (below the dotted line), indicative of the increased charge separation expected in a heterostructure with equal electron and hole transfer. For 480 nm excitation, only electron transfer from the



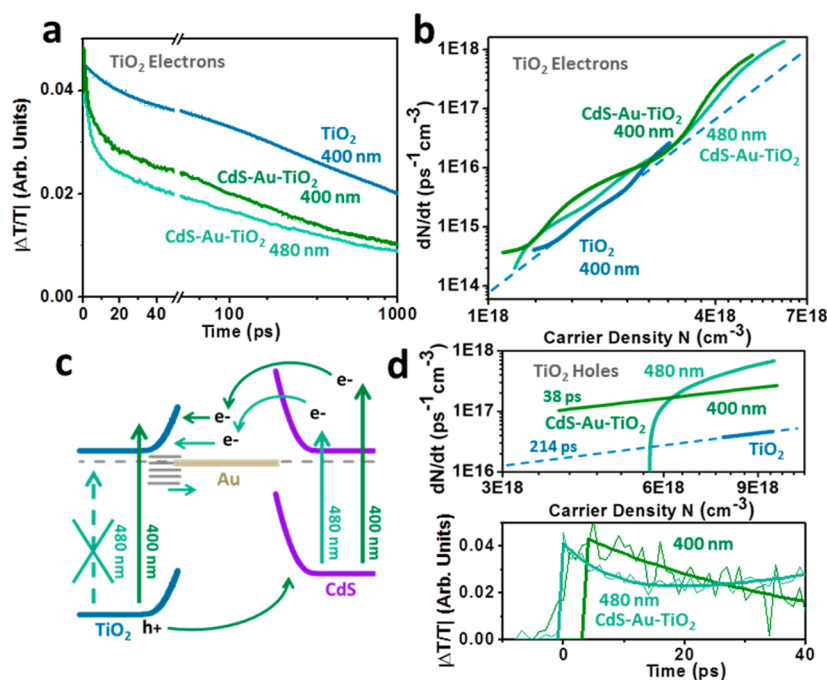


**Figure 6.** Relaxation dynamics in the CdS-Au-TiO<sub>2</sub> heterostructure. (a) Transient absorption decay dynamics for TiO<sub>2</sub> alone and CdS-Au-TiO<sub>2</sub> with a 400 and 480 nm excitation while probing the electron-trap states in TiO<sub>2</sub>. (b) The inverted transient absorption decay showing the underlying form of the rate equation in the acceptor. The trap-state Auger-scattering rate is decreased, the coupling time is increased, and the effective donor lifetime is increased compared to CdS-TiO<sub>2</sub>. (c) proving that the Au is acting as an electron relay and prolonging the carrier lifetime. (d) The decrease in lifetime of the TiO<sub>2</sub> holes probed at the hole-trap states absorption is consistent with charge transfer out of the donor in the heterostructure at 400 nm. At 480 nm the hole states undergo a fast equilibration, consistent with the interfacial Schottky barrier modifying the trap-state occupation and dynamics.

CdS exists (i.e., no hole transfer as seen in Figure 4d), creating a charge imbalance and back-transfer dynamics, as reflected in the decrease in long-time scale lifetime (Figure 4b).

The constant change in rates and lifetimes measured for the CdS and TiO<sub>2</sub> hole donor states suggest the transfer mechanism is first order (illustrated by curved arrows in Figure 4c). The inverted data for the TiO<sub>2</sub> acceptor states, however, show that the initial transfer into the metal-oxide acceptor is faster than the lifetime of TiO<sub>2</sub> alone. This result is contrary to a first-order rate-equation model (Figure 5a,c) and instead suggests a nonlinear dependence of the initial transfer. Nonlinear transfer behavior explains the apparent disagreement between extracted charge-transfer times when measured from the donor and the acceptors separately, since the acceptor decay dynamics occur at a different rate than the change in the donor's lifetime, Supporting Information. The upward trend in the rate can only be replicated if a second-order relaxation term is included in the rate equation of the acceptor (Figure 5b,d), which corresponds to either radiative relaxation or trap-state Auger scattering (Figure S10). Given the long radiative lifetime of TiO<sub>2</sub>, the relaxation mechanism can be assigned to trap-state Auger scattering.<sup>61–63,65</sup> In trap-state Auger scattering an electron relaxes from the CB to a trap state, with the relaxation occurring by giving the excess energy to second electron in the CB. In contrast, Auger scattering occurs by an electron in the CB and a hole in the VB recombining by giving their energy to a second electron or hole. Since the trap-state density is constant, trap-state Auger scattering is second order in carrier density compared to third order in Auger scattering.

The fact that trap-based Auger scattering is a critical part of carrier transfer is not surprising since trap states are known to dominate relaxation dynamics in the heterostructure.<sup>23,66</sup> When

an organic dye is coupled to a semiconductor, the discrete nature of the molecular electronic structure allows the coupling to be well determined by Marcus theory, and a first-order coupled rate equation is frequently applicable to the resulting decay dynamics since the molecular structure of the organic dye prevents the addition of a large density of surface states. On the other hand, the semiconductor nature of the QDs makes the formation of a large density of surface states highly likely, even if the metal-oxide semiconductor is crystalline.<sup>66</sup> The high density of interfacial states will control the charge-transfer rate into the bulk of the TiO<sub>2</sub>. Meaning that the decay rate of the exciton bleach is first order into the interfacial trap states, but the remaining dynamics are controlled nonlinearly by subsequent transfer from the interfacial states into the bulk of the semiconductor, as represented by the green arrow in Figure 4c. This transfer process destroys the simple first-order rate equation picture as seen in Figures 4 and 5. The introduction of a nonlinear charge-transfer mechanism with trap states is consistent with results from organic dyes, where the introduction of a large density of defect states in the metal-oxide semiconductor was found to render the measured kinetics indescribable by a first-order coupled rate equation.<sup>67,68</sup>

Trap-state Auger scattering is the dominant mechanism because the increased carrier flow during charge transfer and the increased charge density due to band bending raise the local carrier density in the surface states. This means that even though carrier density remains low in the bulk of the semiconductor and that the relaxation is first order, the charge density at the interface is sufficiently high for a nonlinear recombination mechanism like trap-state Auger scattering to dominate. This phenomenon can be further confirmed by directly pumping TiO<sub>2</sub> at long wavelengths below the band



edge energy (Figure S13) and directly filling the trap states, with the resulting rates again only describable by trap-state Auger scattering and not a third-order nonlinear process, such as conventional Auger scattering (Figure S14). Trap-state Auger scattering is consistent with recent reports of diffusion-based Auger transfer and recombination.<sup>47,48</sup>

The model for the trap-state Auger transfer mechanism is outlined in Figure S15. There are three key parameters: First is the trap-state Auger-scattering time, which determines the curvature of the initial transfer rate (Figure S15a,d). Second is the lifetime of the donor relative to the acceptor, which modifies the rate at the end of transfer from that of the acceptor alone (Figure S15b,e). The lifetime used for the donor is for the last set of states feeding the acceptor. This means that if the QD has surface states, the effective donor lifetime will be that of the surface states and not that of the measured QD bleach. The effective donor lifetime is determined by the transit time from the bulk QD states to the acceptor states. Finally is the transfer rate, which increases the transfer time or even adds in a second transfer curvature in the rate if it is shorter than the trap-state Auger scattering (Figure S15c,f). To fit the 400 and 480 nm data, the coupling time is initially fixed at 70 ps as determined by the change in the CdS lifetime. The fitting curves are shown in Figure S14. For 480 nm excitation, the trap-state Auger-scattering rate is higher,  $1.7 \times 10^{-19}$  to  $5.3 \times 10^{-20} \text{ cm}^3 \text{ ps}^{-1}$  for 400 nm excitation, which is indicative of a faster relaxation. The effective lifetime of the donor differs between the pump wavelengths, represented by the low carrier-density rate after the transfer is complete. Additionally, the effective donor lifetime is 200 ps for 480 nm compared to 500 ps at 400 nm. A summary of the fitted parameters is shown in Table S1.

The wavelength-dependent change in fitted parameters can be understood in terms of the scheme shown in Figure 4c and based on the spectral distribution of transferred carriers presented in Figure S9. For 480 nm excitation, the carriers are excited at the CB edge of CdS and transfer into the TiO<sub>2</sub> trap states, which creates a higher electron density, a faster transfer time, increased trap-state Auger rate, and reduced effective donor lifetime. For 400 nm excitation the carriers are created in the QD CB continuum, then transfer to the TiO<sub>2</sub> CB and trap states, which slows the transfer and leads to a higher effective donor lifetime as observed in Figure 4b. The latter process mimics excitation in TiO<sub>2</sub> for a 400 nm pump and is evident by comparing the spectral distribution of transferred carriers (Figure S9). To completely fit the data for 400 nm excitation the coupling time is found to be 200 ps (as compared to 70 ps before heterostructuring), which further supports the increase in the transfer time for 400 nm excitation compared to the direct transfer for 480 nm excitation.

**Mechanism of Charge Transfer in CdS-Au-TiO<sub>2</sub>.** The inverted transient absorption analysis is next applied to understand the role of the inclusion of Au in the heterostructure. The inverted exponential decays (Figure 6b) show that the electron-trap states in TiO<sub>2</sub> fill quickly followed by a longer decay relative to TiO<sub>2</sub> alone. The corresponding instantaneous lifetime of the electron- and hole-trap states is shown in Figure S12. By comparing Figure 6b to Figure 4b it is seen the presence of the Au affects the response in several respects. Namely, the initial rate at higher carrier densities (above  $4 \times 10^{18} \text{ cm}^{-3}$ ) has a less abrupt curvature than in the CdS-TiO<sub>2</sub> and spans a larger range of excited carrier density from  $3.9 \times 10^{18}$  up to  $7 \times 10^{18} \text{ cm}^{-3}$ . The trap-state Auger-scattering rates are  $5.9 \times 10^{-20}$  and  $6.5 \times 10^{-20} \text{ cm}^3 \text{ ps}^{-1}$  for the

400 and 480 nm pumps, respectively. In particular, the rate at 480 nm excitation is much reduced from CdS-TiO<sub>2</sub>. The effective donor lifetime is found to be 500 ps in both cases, however, this still does not fully account for the rate after transfer is complete (Figure S14), suggesting an additional transfer rate from CdS to Au and Au to TiO<sub>2</sub>. The additional deviation from the model that develops in the low carrier density regime for the CdS-Au-TiO<sub>2</sub> suggests that the transfer from CdS to Au has been extended and that the transfer from Au to TiO<sub>2</sub> is quicker than the Auger-scattering rate (similar to Figure S15c). The transfer range spans a larger carrier density range from  $1 \times 10^{18}$  up to  $3.8 \times 10^{18} \text{ cm}^{-3}$  than the CdS-TiO<sub>2</sub>, which indicates that the Au is promoting the transfer of a larger number of carriers (i.e., the large span of carrier density span) by extending the transfer process. The observed shifts are consistent with those modeled in Figure S15 for an increased transfer rate and reduced trap-based Auger scattering. This result suggests that the Au is acting as an intermediate “relay” for charge transfer from the CdS to TiO<sub>2</sub> (Figure 6c).

Next it is seen that after the transfer from the CdS to the Au to the TiO<sub>2</sub> is complete, the carriers experience a back transfer ended by a long lifetime that approaches or exceeds that of TiO<sub>2</sub> alone (Figure S12). Observing medium-time scale equilibration and long-time scale charge trapping is consistent with the charge-equilibration effects measured for metals in contact with semiconductors.<sup>55,69,70</sup> Interestingly, the Au nanoparticles remove the long-time scale decrease in lifetime associated with back transfer in the CdS-TiO<sub>2</sub> for 480 nm excitation. Without the Au nanoparticles, the measured long-time scale, lower carrier density dynamics were dependent heavily on the pump wavelength (Figure 4b). The addition of Au makes the final rate similar at both excitation wavelengths (Figure 6b), further confirming that the Au nanoparticles act as a carriers relay from CdS to TiO<sub>2</sub>. The increase in number, rate, and lifetime independent of excitation wavelength explains the constant enhancement in the IPCE by the Au nanoparticles in the CdS-Au-TiO<sub>2</sub> heterostructure for excitation with wavelengths shorter than 525 nm (Figure 3c).

The deviations from the transfer model in the CdS-Au-TiO<sub>2</sub> (Figure S14) are attributed to Au modifying the surface states of both TiO<sub>2</sub> and CdS.<sup>71–77</sup> The modification is evident from suppression of the CdS bleach when Au is added (Figure S9) and is consistent with previous findings.<sup>72,76</sup> The initial analysis supports states in CdS being mixed with (or swamped by) those in the gold, leading to an increased carrier density and increased absorption after the initial excitation is complete. This effect is further illustrated by comparing the rate of carrier relaxation in Au-TiO<sub>2</sub> to CdS-Au-TiO<sub>2</sub> in Figure S16 against the original TiO<sub>2</sub> rates, where the shifts indicate a change in interfacial charge density and trap occupation with the addition of Au/TiO<sub>2</sub> Schottky barrier (Figure 6c). The effect of the Schottky barrier is further evidenced in the dynamics of the hole states (Figure 6d). For 400 nm excitation, the hole transfer rate is 46 ps with a long rise time, slightly faster than the system without the Au (Figure 4d). However, for 480 nm excitation, a higher initial relaxation rate followed by a fast back transfer is measured, represented as a divergence in the rate of Figure 6d. This behavior is consistent with the lack of hole transfer for 480 nm excitation and instead supports charge equilibration at the metal–semiconductor interface. It is unlikely that the transient absorption signal is from Au alone because of the small concentration of Au in the heterostructure and the lack of a

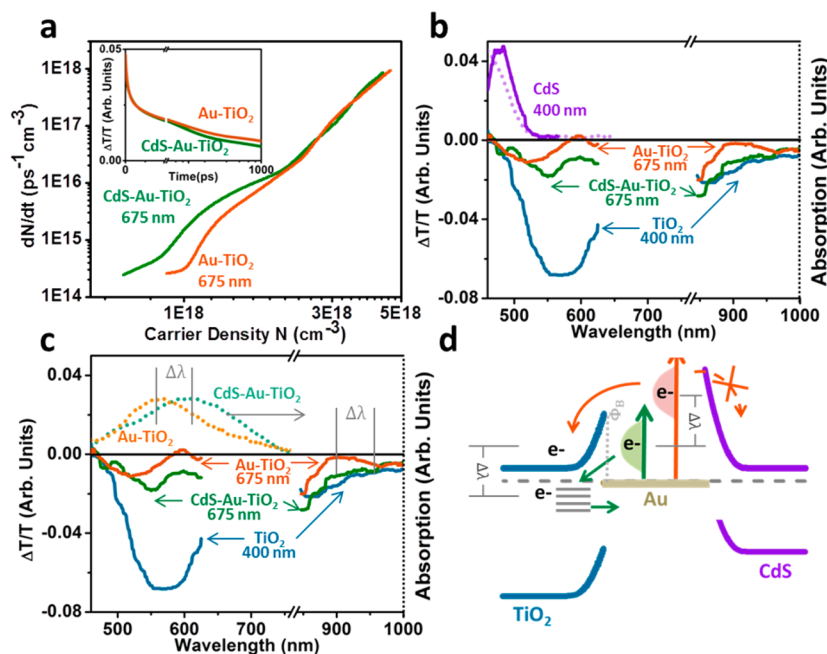


**Figure 7.** Plasmonic energy transfer in CdS-Au-TiO<sub>2</sub>. (a) Dependence of the long time scale decay rate on the plasmon position relative to the 675 nm pump. (b) The full-spectrum transient absorption signal at 20 ps after excitation, showing the lack of CdS bleach for Au-TiO<sub>2</sub> or CdS-Au-TiO<sub>2</sub> which indicates no charge transfer into the CdS. Charge transfer is seen into the TiO<sub>2</sub> electron-trap states. (c) The shift in the LSPR between Au-TiO<sub>2</sub> and CdS-Au-TiO<sub>2</sub> corresponds to the shift in the filling of the TiO<sub>2</sub> trap states. (d) The change in back-transfer dynamics and filling of the TiO<sub>2</sub> electron-trap states without charge transfer into CdS is explained by the energy of the hot plasmonic electron distribution relative to the interfacial Schottky barrier,  $\Phi_B$ .

measurable plasmon bleach for both 400 and 480 nm excitation (illustrated in Figure S9d).

**Mechanism of Plasmonic Energy Transfer from Au to TiO<sub>2</sub>.** Plasmonic dynamics due to the Au nanoparticles were investigated using a 675 nm pump as this wavelength can excite the LSPR but not the CdS or TiO<sub>2</sub>. Plasmonic transfer is determined by measuring the corresponding rise in CdS or TiO<sub>2</sub> excited state when the plasmon is excited. The charge transfer is similar to that of Figures 4 and 6 but with the plasmon now acting as the donor and both semiconductors as acceptors, Figure 7d. The plasmon in the Au-TiO<sub>2</sub> and CdS-Au-TiO<sub>2</sub> is shifted spectrally, from 550 to 600 nm in (Figure S5), allowing differentiation between the plasmonic energy-transfer mechanisms since PIRET and DET differ according to the spectral overlap and hot electron distribution, respectively. Figure 7b shows that exciting the LSPR leads to strong absorption in the TiO<sub>2</sub> electron-trap states only, with a smaller change observed in the crossover region between trapped holes and trapped electrons. No change is seen in the CdS bleach/absorption region when the LSPR is pumped, with the transient absorption signal replicating TiO<sub>2</sub> alone and not CdS-Au-TiO<sub>2</sub> with a 400 or 480 nm excitation wavelength. Given that no spectral overlap exists between TiO<sub>2</sub> and the LSPR, the plasmonic energy-transfer mechanism can only be hot electron transfer by DET. This is further confirmed by the larger percentage of transferred electrons with little change in the trapped hole states (Figure 7c), as PIRET would have led to an equal number of electron and hole pairs being created through resonant interband transitions in the semiconductor.

DET is proposed to occur by transfer of the hot electrons over the interfacial Schottky barrier (Figure 7d).<sup>25,27–31,78,79</sup> The effects of the Schottky barrier on hot electron transfer can be directly measured by comparing the shift in the excited

spectral distribution versus the plasmon shift in the Au-TiO<sub>2</sub> and CdS-Au-TiO<sub>2</sub>. Figure 7c shows the transferred carrier distribution in the CdS-Au-TiO<sub>2</sub> fills the electron-trap states higher in wavelength than the Au-TiO<sub>2</sub>. The shift in the transferred electron distribution is similar to the plasmon redshift. This occurs because the hot plasmonic electrons in the Au-TiO<sub>2</sub> system have a higher energetic offset from the Au Fermi level due to the blue-shifted plasmon peak and can therefore more effectively overcome the interfacial Schottky barrier to transfer into the TiO<sub>2</sub> CB (Figure 7d). The CdS-Au-TiO<sub>2</sub> has a red-shifted plasmon with a smaller energy offset from the Au Fermi level; it therefore cannot effectively overcome the interfacial Schottky barrier, instead transferring electrons to the trap states in TiO<sub>2</sub> below the CB (Figure 7d). In neither case do the carriers appear to have enough energy to efficiently transfer into the CdS.

The effect of offset hot electron energy from the Schottky barrier is also seen in the inverted transient absorption data (Figure 7a) and instantaneous lifetime (Figure S12). The electron transfer is similar on short time scales for both heterostructures. However, at long time scale, the carriers in the CdS-Au-TiO<sub>2</sub> have a shorter lifetime because they can transfer into the interfacial trap states and quickly transfer back into the Au. In comparison, the Au-TiO<sub>2</sub> plasmonic electrons have a longer lifetime because they can become trapped behind the interfacial Schottky barrier. The back transfer in the CdS-Au-TiO<sub>2</sub> may explain the small increase in the overall IPCE despite the large increase in absorption due to the plasmon (Figure 2). If the plasmonic electrons are to be used more efficiently, the transferred charge carriers need to be trapped behind the Schottky barrier so they can be extracted before recombination.

**Dual Role of Au Nanoparticle.** The inversion analysis method for transient absorption spectroscopy has revealed the

critical role that the interfacial trap states play in the CdS-TiO<sub>2</sub>, the effect of Au on interfacial transfer and long-time scale back transfer, and the effect of the plasmonic hot electron energy relative to the interfacial Schottky barrier. Using this information, the PEC performance can be accurately described by Figure 8.

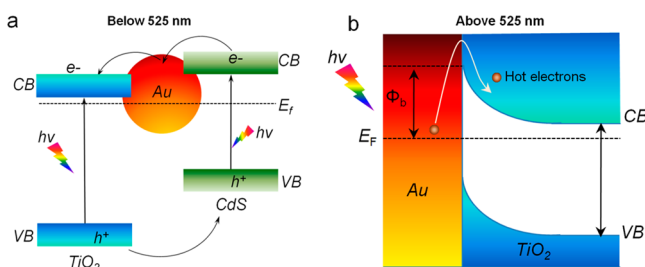


**Figure 8.** Wavelength-dependent dual role of Au nanoparticles in the CdS-Au-TiO<sub>2</sub> sandwich structure. (a) Electron relay effect of Au nanoparticles, facilitating the charge transfer from CdS QDs to TiO<sub>2</sub> nanorod under the irradiation of incident solar light with the wavelength  $<525$  nm. (b) Plasmonic energy transfer from the excited Au nanoparticles to TiO<sub>2</sub> through the hot electrons transfer under the irradiation of incident solar light with the wavelength  $>525$  nm. CB = conduction band, VB = valence band,  $E_F$  = Fermi energy level, and  $\Phi_B$  = Schottky barrier.

At incident light wavelengths shorter than 525 nm, the LSPR in the Au nanoparticles is not excited. Hence the photocurrent enhancement is not due to the LSPR of Au nanoparticles. Instead, charge carriers are created in the CdS QDs (Figure 2). The photogenerated charge carriers transfer from the CdS QDs to TiO<sub>2</sub> via the Au nanoparticles as shown in Figure 8a. At wavelengths longer than 525 nm, the energy of the light is insufficient to create carriers in the TiO<sub>2</sub> or CdS (Figure 2), hence no charge transfer occurs from CdS to TiO<sub>2</sub>. However, the LSPR is excited in the Au nanoparticles. As reported previously,<sup>25</sup> when the plasmonic Au nanoparticles are in intimate contact with TiO<sub>2</sub>, hot electrons are excited and can transfer from the plasmonic metal to the conduction band of TiO<sub>2</sub> as shown in Figure 8b. In this case, the Au nanoparticles act as the plasmonic photosensitizer, increasing photo-conversion in the wavelength from 525 to 725 nm. This is confirmed by the variation in IPCE and IPCE enhancement factor at wavelengths corresponding to the LSPR from 525 to 725 nm (Figure 3b,c).

## CONCLUSIONS

In summary, the gold nanoparticles sandwiched between the TiO<sub>2</sub> nanorod and the CdS QD layer played a dual role in enhancing the solar-to-chemical energy conversion efficiency of PEC. The function of the Au nanoparticles depended on the incident light wavelength relative to the plasmon. Upon irradiation at the wavelengths shorter than 525 nm, the charge carriers were generated in the CdS QDs but not in the plasmon. In this case, the Au nanoparticles served as an electron relay of charge carriers between the CdS QDs and TiO<sub>2</sub>. At the wavelength range of 525–725 nm, the CdS QDs were unable to serve as a photosensitizer, but the LSPR was excited in the Au nanoparticles that acted as a plasmonic photosensitizers, injecting hot electrons into the TiO<sub>2</sub>. The combination of the charge-transfer enhancement and the light absorption bandwidth extension in a single structure was

responsible for the improvement in the solar-to-chemical energy conversion efficiency.

An inversion transient absorption analysis method combined with a white-light probe unraveled the key role that the interfacial trap states and the trap-state Auger recombination played during the processes of charge transfer between CdS and TiO<sub>2</sub>. By including the Au nanoparticles in the heterostructure, it was found that (i) the rate of trap-state Auger recombination decreased, (ii) the number of charge carriers transferred increased, (iii) the rate of transfer increased, and (iv) the charge separation was prolonged, even at the point of suppressing the back transfer when only CdS was excited. The Au nanoparticles were therefore found to eliminate some of the deficiencies caused by interfacial trap states, which improved the photoelectrochemical performance as demonstrated in the IPCE. For these materials, the plasmonic energy-transfer mechanism was proven to be DET, with the rate of charge transfer and back transfer dependent on the relative energy of the hot plasmonic electrons to the Schottky barrier. This study has provided a new facile and efficient strategy for optimization of photoelectrode architecture using already known materials.

## ASSOCIATED CONTENT

### Supporting Information

Detailed description on the motivation, explanation, and implementation of the pump–probe inversion analysis, procedure for applying the inversion analysis, transient absorption, SEM, TEM, XPS, and solar-to-chemical conversion efficiency. This material is available free of charge via the Internet at <http://pubs.acs.org>.

## AUTHOR INFORMATION

### Corresponding Author

[nick.wu@mail.wvu.edu](mailto:nick.wu@mail.wvu.edu)

### Author Contributions

<sup>||</sup>These authors contributed equally.

### Notes

The authors declare no competing financial interest.

## ACKNOWLEDGMENTS

This work was supported by the National Science Foundation (CBET-1233795) and NSF Graduate Research Fellowship (1102689). The resource and facilities used were partially supported by NSF (EPS 1003907), the West Virginia University Research Corporation EPSCoR Grant. The use of WVU Shared Facility was appreciated.

## REFERENCES

- (1) Grätzel, M. *Nature* **2001**, *414*, 338–344.
- (2) Walter, M. G.; Warren, E. L.; McKone, J. R.; Boettcher, S. W.; Mi, Q.; Santori, E. A.; Lewis, N. S. *Chem. Rev.* **2010**, *110*, 6446–6473.
- (3) Tachibana, Y.; Vayssieres, L.; Durrant, J. *Nat. Photonics* **2012**, *6*, 511–518.
- (4) Katz, M. J.; Riha, S. C.; Jeong, N. C.; Martinson, A. B. F.; Farha, O. K.; Hupp, J. T. *Coord. Chem. Rev.* **2012**, *256*, 2521–2529.
- (5) Osterloh, F. E. *Chem. Soc. Rev.* **2013**, *42*, 2294–2320.
- (6) Osterloh, F. E.; Parkinson, B. A. *MRS Bull.* **2011**, *36*, 17–22.
- (7) Wu, N. Q.; Wang, J.; Tafen, D. N.; Wang, H.; Zheng, J.; Lewis, J. P.; Liu, X.; Leonard, S. S.; Manivannan, A. *J. Am. Chem. Soc.* **2010**, *132*, 6679–6685.
- (8) Wang, J.; Tafen, D. N.; Lewis, J. P.; Hong, Z.; Manivannan, A.; Zhi, M.; Li, M.; Wu, N. Q. *J. Am. Chem. Soc.* **2009**, *131*, 12290–12297.



- (9) Meng, F.; Hong, Z.; Arndt, J.; Li, M.; Zhi, M.; Yang, F.; Wu, N. Q. *Nano Res.* **2012**, *5*, 213–221.
- (10) Yang, C.; Wang, Z.; Lin, T.; Yin, H.; Lv, X.; Wan, D.; Xu, T.; Zheng, C.; Lin, J.; Huang, F.; Xie, X.; Jiang, M. *J. Am. Chem. Soc.* **2013**, *135*, 17831–17838.
- (11) Asahi, R.; Morikawa, T.; Ohwaki, T.; Aoki, K.; Taga, Y. *Science* **2001**, *293*, 269–271.
- (12) Sakthivel, S.; Kisch, H. *Angew. Chem., Int. Ed.* **2003**, *42*, 4908–4911.
- (13) Chen, H.; Chen, C. K.; Chang, Y.; Tsai, C.; Liu, R.; Hu, S.; Chang, W.; Chen, K. *Angew. Chem., Int. Ed.* **2010**, *49*, 5966–5969.
- (14) Wang, H.; Wang, G.; Ling, Y.; Lepert, M.; Wang, C.; Zhang, J.; Li, Y. *Nanoscale* **2012**, *4*, 1463–1466.
- (15) Wang, G.; Yang, X.; Qian, F.; Zhang, J.; Li, Y. *Nano Lett.* **2010**, *10*, 1088–1092. Hensel, J.; Wang, G.; Li, Y.; Zhang, J. *Nano Lett.* **2010**, *10*, 478–483.
- (16) Buhbut, S.; Itzhakov, S.; Hod, I.; Oron, D.; Zaban, A. *Nano Lett.* **2013**, *13*, 4456–4461.
- (17) Kamat, P. V.; Tvrđy, K.; Baker, D. R.; Radich, J. G. *Chem. Rev.* **2010**, *110*, 6664–6688.
- (18) Kamat, P. V. *J. Phys. Chem. C* **2007**, *111*, 2834–2860.
- (19) Berea, E. M.; Shalom, M.; Gimenez, S.; Hod, I.; Mora-Sero, I.; Zaban, A.; Bisquert, J. *J. Am. Chem. Soc.* **2010**, *132*, 6834–6839.
- (20) Gonzalez-Pedro, V.; Xu, X.; Mora-Sero, I.; Bisquert, J. *ACS Nano* **2010**, *4*, 5783–5790.
- (21) Chakrapani, V.; Baker, D.; Kamat, P. V. *J. Am. Chem. Soc.* **2011**, *133*, 9607–9615.
- (22) Hyun, B.; Zhong, Y.; Bartnik, A. C.; Sun, L.; Abruña, H. D.; Wise, F. W.; Goodreau, J. D.; Matthews, J. R.; Leslie, T. M.; Borrelli, N. F. *ACS Nano* **2008**, *2*, 2206–2212.
- (23) Shalom, M.; Tachan, Z.; Bouhadana, Y.; Barad, H.; Zaban, A. *J. Phys. Chem. Lett.* **2011**, *2*, 1998–2003.
- (24) Cushing, S. K.; Wu, N. Q. *Interface* **2013**, *22*, 63–67.
- (25) Tian, Y.; Tatsuma, T. *J. Am. Chem. Soc.* **2005**, *127*, 7632–7637. Tian, Y.; Tatsuma, T. *Chem. Commun.* **2004**, 1810–1811.
- (26) Cushing, S. K.; Li, J.; Meng, F.; Senty, T. R.; Suri, S.; Zhi, M.; Li, M.; Bristow, A. D.; Wu, N. Q. *J. Am. Chem. Soc.* **2012**, *134*, 15033–15041.
- (27) Chen, H.; Chen, C. K.; Chen, C. J.; Cheng, L.; Wu, P.; Cheng, B.; Ho, Y.; Tseng, M.; Hsu, Y.; Chan, T.; Lee, J.; Liu, R.; Tsai, D. *ACS Nano* **2012**, *6*, 7362–7372.
- (28) Chen, H.; Chen, C. K.; Tseng, M.; Wu, P.; Chang, C.; Cheng, L.; Huang, H.; Chan, T.; Huang, D.; Liu, R.; Tsai, D. *Small* **2013**, *9*, 2926–2936.
- (29) Mubeen, S.; Hernandez-Sosa, G.; Moses, D.; Lee, J.; Moskovits, M. *Nano Lett.* **2011**, *11*, 5548–5552.
- (30) Liu, Z.; Hou, W.; Pavaskar, P.; Aykol, M.; Cronin, S. B. *Nano Lett.* **2011**, *11*, 1111–1116.
- (31) Warren, S.; Thimsen, E. *Energy Environ. Sci.* **2012**, *5*, 5133–5146.
- (32) Li, J.; Cushing, S.; Bright, J.; Meng, F.; Senty, T. R.; Zheng, P.; Bristow, A. D.; Wu, N. Q. *ACS Catalysis* **2013**, *3*, 47–51.
- (33) Li, J.; Cushing, S. K.; Zheng, P.; Meng, F.; Chu, D.; Wu, N. Q. *Nat. Commun.* **2013**, *4*, 2651.
- (34) Tada, H.; Mitsui, T.; Kiyonaga, T.; Akita, T.; Tanaka, K. *Nat. Mater.* **2006**, *5*, 782–786.
- (35) Yun, H. J.; Lee, H.; Kim, N. D.; Lee, D. M.; Yu, S.; Yi, J. *ACS Nano* **2011**, *5*, 4084–4090.
- (36) Fang, J.; Zhang, Z.; Yuan, Y.; Cao, S.; Wang, Z.; Yin, L.; Xiao, Y.; Xue, C. *ACS Appl. Mater. Interfaces* **2013**, *5*, 8088–8092. Yu, Z.; Xie, Y.; Liu, G.; Lu, G.; Ma, X.; Chen, H. *J. Mater. Chem. A* **2013**, *1*, 2773–2776.
- (37) Lv, T.; Pan, L.; Liu, X.; Sun, Z. *Electrochim. Acta* **2012**, *83*, 216–220.
- (38) Zhu, H.; Yang, B.; Xu, J.; Fu, Z.; Wen, M.; Guo, T.; Fu, S.; Zuo, J.; Zhang, S. *Appl. Catal., B* **2009**, *90*, 463–469.
- (39) Cánovas, E.; Moll, P.; Jensen, S. A.; Gao, Y.; Houtepen, A. J.; Siebbeles, L. D. A.; Kinger, S.; Bonn, M. *Nano Lett.* **2011**, *11*, 5234–5239.
- (40) Tisdale, W. A.; Williams, K. J.; Timp, B. A.; Norris, D. J.; Aydil, E. S.; Zhu, X. Y. *Science* **2010**, *328*, 1543–1547.
- (41) Shen, Q.; Ayuzawa, Y.; Katayama, K.; Sawada, T.; Toyoda, T. *Appl. Phys. Lett.* **2010**, *97*, 263113.
- (42) Blackburn, J. L.; Selmarten, D. C.; Nozik, A. J. *J. Phys. Chem. B* **2003**, *107*, 14154–14157.
- (43) Blackburn, J. L.; Selmarten, D. C.; Ellingson, R. J.; Jones, M.; Micic, O.; Nozik, A. J. *J. Phys. Chem. B* **2005**, *109*, 2625–2631.
- (44) Tvrđy, K.; Frantsuzov, P. A.; Kamat, P. V. *Proc. Natl. Acad. Sci. U. S. A.* **2011**, *108*, 29–34.
- (45) Jin, S.; Lian, T. *Nano Lett.* **2009**, *9*, 2448–2454.
- (46) Pernik, D.; Tvrđy, K. *J. Phys. Chem. C* **2011**, *115*, 13511–13519.
- (47) Gao, Y.; Suchand Sandeep, C. S.; Schins, J. M.; Houtepen, A. J.; Siebbeles, L. D. A. *Nat. Commun.* **2013**, *4*, 2329.
- (48) Zhu, H.; Yang, Y.; Hyeon-Deuk, K.; Califano, M.; Song, N.; Wang, Y.; Zhang, W.; Prezhdo, O. V.; Lian, T. *Nano Lett.* **2014**, *14*, 1263–1269.
- (49) Liu, B.; Aydil, E. S. *J. Am. Chem. Soc.* **2009**, *131*, 3985–3990.
- (50) Li, J.; Hoffmann, M. W. G.; Shen, H.; Fabrega, C.; Prades, J. D.; Andreu, T.; Hernandez-Ramirez, F.; Mathur, S. J. *Mater. Chem.* **2012**, *22*, 20472–20476.
- (51) Pu, Y.; Wang, G.; Chang, K.; Ling, Y.; Lin, Y.; Fitzmorris, B. C.; Liu, C.; Lu, X.; Tong, Y.; Zhang, J. Z.; Hsu, Y.; Li, Y. *Nano Lett.* **2013**, *13*, 3817–3823.
- (52) Li, J.; Meng, F.; Suri, S.; Ding, W.; Huang, F.; Wu, N. *Chem. Commun.* **2012**, *48*, 8213–8215. Meng, F.; Li, J.; Cushing, S. K.; Zhi, M.; Wu, N. *J. Am. Chem. Soc.* **2013**, *135*, 10286–10289. Schmuki, P.; Böhm, H.; Bardwell, J. A. *J. Electrochem. Soc.* **1995**, *142*, 1705–1712.
- (53) Gao, H.; Jeong, H.; Yang, P. *ACS Nano* **2012**, *6*, 234–240.
- (54) Jakob, M.; Levanon, H.; Kamat, P. *Nano Lett.* **2003**, *3*, 353–358.
- (55) Subramanian, V.; Wolf, E. E.; Kamat, P. *J. Am. Chem. Soc.* **2004**, *126*, 4943–4950.
- (56) Bahnemann, D. *J. Phys. Chem. B* **1997**, *101*, 4265–4275.
- (57) Katoh, R.; Murai, M.; Furube, A. *Chem. Phys. Lett.* **2010**, *500*, 309–312.
- (58) Tamaki, Y.; Hara, K.; Katoh, R. *J. Phys. Chem. C* **2009**, *113*, 11741–11746.
- (59) Tamaki, Y.; Furube, A.; Murai, M.; Hara, K.; Katoh, R.; Tachiya, M. *Phys. Chem. Chem. Phys.* **2007**, *9*, 1453–1460.
- (60) Yoshihara, T.; Katoh, R.; Furube, A. *J. Phys. Chem. B* **2004**, *108*, 3817–3823.
- (61) Linnros, J. *J. Appl. Phys.* **1998**, *84*, 275.
- (62) Linnros, J. *J. Appl. Phys.* **1998**, *84*, 284.
- (63) Grivickas, V.; Linnros, J. In *Characterization of Materials*; John Wiley and Sons, Inc.: Hoboken, NJ, 2012; p 658.
- (64) Froitzheim, A.; Stangl, R.; Elstner, L.; Krieger, M.; Fuhs, W. Proceedings of the 3rd World Conference on Photovoltaic Energy Conversion, Osaka, Japan, May 11–13, 2003; WCPEC-3 Organizing Committee: Japan, 2003; pp 279–282.
- (65) Landsberg, P. *Appl. Phys. Lett.* **1987**, *50*, 745–747.
- (66) Markus, T.; Itzhakov, S. *J. Phys. Chem. C* **2011**, *115*, 13236–13241.
- (67) Hao, E.; Anderson, N. *J. Phys. Chem. B* **2002**, *106*, 10191–10198.
- (68) Bisquert, J.; Zaban, A.; Salvador, P. *J. Phys. Chem. B* **2002**, *106*, 8774–8782.
- (69) Hirakawa, T.; Kamat, P. *Langmuir* **2004**, *20*, 5645–5647.
- (70) Choi, H.; Chen, W.; Kamat, P. *ACS Nano* **2012**, *6*, 4418–4427.
- (71) Khon, E.; Mereshchenko, A.; Tarnovsky, A. N.; Acharya, K.; Klinkova, A.; Hewa-Kasakarage, N. N.; Nemitz, I.; Zamkov, M. *Nano Lett.* **2011**, *11*, 1792–1799.
- (72) Kobayashi, Y.; Nonoguchi, Y.; Wang, L.; Kawai, T.; Tamai, N. *J. Phys. Chem. Lett.* **2012**, *3*, 1111–1116.
- (73) Dreaden, E. C.; Neretina, S.; Qian, W.; El-Sayed, M. A.; Hughes, R. A.; Preston, J. S.; Mascher, P. *J. Phys. Chem. C* **2011**, *115*, 5578–5583.
- (74) Zhang, W.; Govorov, A.; Bryant, G. *Phys. Rev. Lett.* **2006**, *97*, 146804.
- (75) Artuso, R. D.; Bryant, G. W. *Phys. Rev. B* **2010**, *82*, 195419.



(76) Mongin, D.; Shaviv, E.; Maioli, P.; Crut, A.; Banin, U.; Del Fatti, N.; Vallée, F. *ACS Nano* **2012**, *6*, 7034–7043.

(77) Wu, K.; Rodríguez-Córdoba, W. E.; Yang, Y.; Lian, T. *Nano Lett.* **2013**, *13*, 5255–5263.

(78) Govorov, A. O.; Zhang, H.; Gun'ko, Y. K. *J. Phys. Chem. C* **2013**, *117*, 16616–16631.

(79) Govorov, A. O.; Carmeli, I. *Nano Lett.* **2007**, *7*, 620–625.